Effects of Oxygen Concentration on the Reactive Oxygen Species Density Under Different Operating Conditions in Atmospheric-Pressure Helium/Oxygen Pulsed Dielectric Barrier Discharge

XIAOLONG WANG[1], YADI LIU[1], ZHENYU TAN[1], AND LILI CHANG[2,3]

[1]Shandong Provincial Key Laboratory of UHV Transmission Technology and Equipment, School of Electrical Engineering, Shandong University, Jinan 250061, China
[2]School of Materials Science and Engineering, Shandong University, Jinan 250061, China
[3]Key Laboratory for Liquid-Solid Structure Evolution and Processing of Materials, Ministry of Education, Shandong University, Jinan 250061, China

Corresponding author: Xiaolong Wang (wangxiaolong@sdu.edu.cn)

ABSTRACT In this paper, a numerical investigation on the effects of oxygen concentration on the reactive oxygen species (ROS) density under different operating conditions in the atmospheric-pressure helium/oxygen pulsed dielectric barrier discharge (DBD) has been performed by means of a one-dimensional (1-D) fluid model. The involved ROS are ground state oxygen atom O, excited state oxygen atom $O(^1D)$, single delta metastable oxygen $O_2(^1\Delta g)$ (SDO), and ozone molecule O_3. The present work gives the following significant results. For a given operating condition, the averaged O density is evidently larger than the other three ROS densities. There exist characteristic oxygen concentrations where the averaged densities of O and SDO reach their maximum with the increase in the oxygen concentration, respectively. The averaged O_3 density increases with the oxygen concentration, but the reverse is true for the averaged $O(^1D)$ density. In addition, the ROS density is increased when increasing the applied voltage amplitude V_a, decreasing the rising time of the applied voltage pulse t_r, or reducing the frequency of the applied voltage pulse f. Also, the characteristic oxygen concentrations for the averaged densities of both the O and SDO move towards the higher oxygen concentration when increasing the V_a, decreasing the t_r, or increasing the f. The effect of the operating conditions on the averaged O_3 density is weak under lower oxygen concentrations, and it is increasingly affected by the operating conditions with the increasing oxygen concentration. However, the variation trend of the averaged $O(^1D)$ density versus oxygen concentration is hardly affected by the operating conditions.

INDEX TERMS Helium/oxygen, pulsed dielectric barrier discharge, oxygen concentration effect, one-dimensional fluid model.

I. INTRODUCTION

In recent years, atmospheric-pressure low-temperature plasmas have been receiving attention because of their great potential in various fields, including material processing [1]–[4], environmental remediation [5]–[8], plasma assisted combustion [9], [10], and biomedicine [11]–[13]. A popular way of generating this type of plasmas is to make use of the dielectric barrier discharge (DBD). Compared with the DBD driven by continuous sinusoidal voltages, the DBD excited by repetitive voltage pulses can effectively improve the stability and chemical activity of the plasma and produce high electron energy, uniform and larger area of non-equilibrium plasma [14]–[16].

The addition of oxygen to the working gas can affect plasma chemistry and produce large amounts of reactive oxygen species (ROS), such as ground state oxygen atom O, excited state oxygen atom $O(^1D)$, single delta metastable

The associate editor coordinating the review of this manuscript and approving it for publication was Giambattista Gruosso.

oxygen $O_2(^1\Delta g)$ (SDO), and ozone molecule O_3, etc [17]. It has been shown that the ROS may be delivered to the surface or interior of living cells, and play an essential role in biomedicine including wound treatment, dermatological therapy, and medical device disinfection [18]. Consequently, the generation mechanism and the control of the ROS have been investigated by many research groups [19]–[22]. Using a one-dimensional fluid model, the mode transition of dielectric barrier discharge in atmospheric-pressure helium-oxygen mixture has been simulated by Lee *et al.* [19], and it was pointed that when oxygen is rare, the discharge has similar characteristics to the direct current glow discharge at low pressure. As the oxygen additive increases, the discharge characteristics of the glow mode are destroyed and changed into the Townsend mode. In the work of Alshraiedeh *et al.* [20], the effect of oxygen concentration on virucidal activity in nonthermal plasma inactivation of MS2 bacteriophage has been studied, and it was indicated that the optimal inactivated oxygen concentration is 0.75%. The inactivation of resistant *Candida albicans* in a sealed package by cold atmospheric pressure plasmas was carried out by Song *et al.* [21], by means of varying oxygen concentration, the He plasma containing about 1% O_2 was found to entirely kill resistant *Candida albicans* with a treatment time of 5 min. In a previous work [22], the effect of oxygen concentration ranging from 0.1% to 1.1% on the pulsed DBD in helium-oxygen mixture was numerically researched by Wang *et al.*, and it was found that the total density of the reactive oxygen species reaches its maximums at the O_2 concentration of about 0.5%. From what has been introduced above, there exists a characteristic oxygen concentration, corresponding to the best sterilization effect or the highest ROS density. However, the concentration will vary with the operating condition. Therefore, it is essential to investigate the characteristic oxygen concentration and to explore the effect of operating conditions on the oxygen concentration, which plays a significant guiding role for the application of plasma in biomedicine.

In this work, the effects of oxygen concentration on the ROS density under different operating conditions in the atmospheric-pressure helium/oxygen pulsed DBDs have been systematically simulated by means of the numerical simulation based on a one-dimensional (1-D) fluid model. Here, the operating conditions refer to the applied voltage amplitude V_a, rising time of the applied voltage pulse t_r, and frequency of the applied voltage pulse f. Due to the electronegativity of oxygen, the pulsed DBDs in helium-oxygen mixtures are usually investigated at the oxygen concentrations below about 1%, and in this work, therefore, the considered oxygen concentrations are in the range from 0.1% to 1%.

II. SIMULATION MODEL
The parallel-plate plasma reactor and the simulation model used in the present work are the same as those in the previous works [22]–[24] where the model consists of the
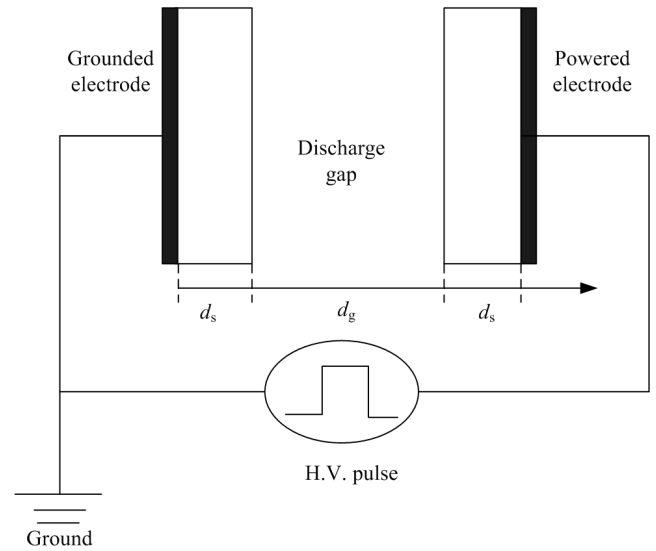

FIGURE 1. Schematic of the DBDs driven by high-voltage pulses at atmospheric pressure. d_g and d_s are the gap width and dielectric thickness, respectively.

1-D continuity equation, the electron energy equation, and the current conservation equation. Thus, only a brief description for this model is given for completeness.

As presented in Fig. 1, the atmospheric pressure DBD is sustained between two parallel-plate electrodes, and each electrode is covered with dielectric. For the two electrodes, one is the grounded (grounded electrode) and the other (powered electrode) is of the applied voltage.

The dynamic behaviors of electrons, ions, and neutral particles are described by the 1-D continuity equation

$$\frac{\partial n_{e,i,*}}{\partial t} + \frac{\partial \Gamma_{e,i,*}}{\partial x} = S_{e,i,*} \tag{1}$$

where n is the particle number density, Γ is the particle flux density, S denotes the particle source term, and subscripts e, i, $*$ represent electrons, helium and oxygen related ions, and neutral particles, respectively. The neutral particles include molecules, atoms, excited and metastable species of helium and oxygen.

The particle flux densities under the drift-diffusion approximation are given by

$$\Gamma_e = -\mu_e E n_e - D_e \frac{\partial n_e}{\partial x} \tag{2}$$

$$\Gamma_i = -\mu_i E n_i - D_i \frac{\partial n_i}{\partial x} \tag{3}$$

$$\Gamma_* = -D_* \frac{\partial n_*}{\partial x} \tag{4}$$

where μ is the mobility, D is the diffusion coefficient, and E is the electric field. For the neutral particle, only diffusion item ought to be considered in the flux.

The electron energy equation of describing the electron temperature can be expressed as

$$\frac{\partial (\frac{3}{2}kT_e n_e)}{\partial t} + \frac{\partial Q}{\partial x} + e\Gamma_e E + e\sum \Delta \varepsilon_i r_i = 0 \tag{5}$$

where k is the Boltzmann constant, r_i is the reaction rate of the ith reaction, $\Delta\varepsilon_i$ is the threshold energy of the inelastic collision caused by the ith reaction, T_e is the electron temperature, and the electron energy flux Q is obtained from

$$Q = -\lambda_e \frac{\partial T_e}{\partial x} + \frac{5}{2} k T_e \Gamma_e \qquad (6)$$

where λ_e is given by

$$\lambda_e = \frac{5}{2} k D_e n_e \qquad (7)$$

The electric field E is obtained by the current conservation equation, taking the form of

$$\frac{\partial E}{\partial t} = \frac{J_0(t)}{\varepsilon_0} - \frac{e}{\varepsilon_0}(\Gamma_i - \Gamma_e) \qquad (8)$$

with

$$J_0(t) = \left(-\varepsilon_0 \frac{\partial V_a(t)}{\partial t} + \int_0^{d_g} J_g(x,t)\mathrm{d}x\right) / \left(d_g + \frac{2d_s}{\varepsilon_r}\right) \qquad (9)$$

where ε_0 is the permittivity of free space, V_a is the applied voltage, J_g is the discharge current density, d_g is the gap width, d_s is the dielectric thickness, and ε_r is the dielectric constant.

Considering the effect of the secondary electron emission, the total electron flux density Γ_e' at the cathode surface can be given by

$$\Gamma_e' = \Gamma_e - \gamma \sum_i \Gamma_i \qquad (10)$$

where γ is the emission coefficient of the secondary electron at dielectric surface due to ion impact.

According to He and Zhang [25], in this work, 17 key species and 48 chemical reactions are taken into account for high computational efficiency. In addition to the ground state atoms He and ground state molecules O_2, the consideration for the particles generated in the discharge processes in the present simulation is as follows: electrons e, helium atomic ions He^+, helium molecular ion He_2^+, helium metastable atom He^*, helium excimer molecule He_2^*, ground state atomic oxygen O, ozone molecular O_3, excited atomic oxygen $O(^1D)$, single delta metastable oxygen (SDO) $O_2(^1\Delta g)$, singlet sigma metastable oxygen $O_2(^1\Sigma_g^+)$, positive atomic ion O^+, positive molecular ion O_2^+, negative atomic ion O^-, and negative molecular ion O_2^- and O_3^-. The considered chemical reactions as well as the corresponding rate coefficients are listed in Table 1. However, Generally, the cross sections for the collisions between electrons and neutral particles need to be calculated and the complicated calculations for evaluating the reaction rate coefficients are required. This will be considered in the future studies.

To verify the reliability of the present model, the operating parameters are chosen as the same as those in the experiment of experiment of Walsh *et al.* [38], i.e. the dielectric constant $\varepsilon_r = 6.5$, the dielectric thickness $d_s = 0.1$ cm, the secondary electron emission coefficient $\gamma = 0.02$, and

TABLE 1. Key reactions and their rate coefficients in helium/oxygen pulsed DBDS.

| No.	Reaction	Rate coefficient	Energy	Ref.
R1	$e+He\rightarrow He^++2e$	$1.5\times10^{-9}T_e^{0.68}\exp(-24.6/T_e)$	24.6	26
R2	$e+He\rightarrow He^*+e$	$4.2\times10^{-9}T_e^{0.31}\exp(-19.8/T_e)$	19.8	26
R3	$e+He^*\rightarrow He+e$	2.0×10^{-10} cm^{3}s^{-1}		27
R4	$e+He^*\rightarrow He^++2e$	$1.28\times10^{-7}T_e^{0.6}\exp(-4.78/T_e)$	4.78	26
R5	$e+He_2^*\rightarrow He+He+e$	3.8×10^{-9} cm^{3}s^{-1}		28
R6	$e+He_2^*\rightarrow He_2^++2e$	$9.75\times10^{-10}T_e^{0.71}\exp(-3.4/T_e)$	3.4	27
R7	$He_2^*+M\rightarrow He+He+M$	1.0×10^6 cm^{3}s^{-1}		29
R8	$e+He_2^+\rightarrow 2He$	1.0×10^{-8} cm^{3}s^{-1}		30
R9	$e+He_2^+\rightarrow He\rightarrow 3He$	2.0×10^{-27} cm^{3}s^{-1}		30
R10	$e+He_2^+\rightarrow He^*+He^+$	$5.0\times10^{-9}T_e^{-0.5}$ cm^{6}s^{-1}		26
R11	$e+O_2\rightarrow O^-+O$	$8.8\times10^{-11}\exp(-4.4/T_e)$ cm^{3}s^{-1}		31
R12	$e+O_2\rightarrow O+O(^1D)+e$	$5.0\times10^{-8}\exp(-8.4/T_e)$ cm^{3}s^{-1}	8.4	31
R13	$e+O_2(^1\Delta g)\rightarrow e+O_2$	$5.6\times10^{-9}\exp(-2.2/T_e)$ cm^{3}s^{-1}		32
R14	$e+O_2\rightarrow O_2(^1\Delta g)+e$	$1.7\times10^{-9}\exp(-3.1/T_e)$ cm^{3}s^{-1}	3.1	31
R15	$e+O_2\rightarrow O+O^++e$	$7.1\times10^{-11}T_e^{0.5}\exp(-17/T_e)$ cm^{3}s^{-1}		32
R16	$e+O_2\rightarrow 2O+e$	$4.2\times10^{-9}\exp(-5.6/T_e)$ cm^{3}s^{-1}	5.6	32
R17	$e+O_3\rightarrow O_2^-+O$	1.0×10^{-9} cm^{3}s^{-1}		32
R18	$e+O_3\rightarrow O+O_2+e$	$1.0\times10^{-8}(300/T_g)^{0.5}$ cm^{3}s^{-1}		33
R19	$e+O(^1D)\rightarrow e+O$	8.0×10^{-9} cm^{3}s^{-1}		32
R20	$e+O\rightarrow e+O(^1D)$	$4.2\times10^{-9}\exp(-2.25/T_e)$ cm^{3}s^{-1}	2.25	31
R21	$O+O+He\rightarrow O_2+He$	$1.3\times10^{-33}(3000/T_g)\exp(-170/T_g)$		30
R22	$O+O_2+He\rightarrow O_3+He$	6.27×10^{-34} cm^{6}s^{-1}	4.88	28
R23	$O+O_2+O_2\rightarrow O_3+O_2$	$6.9\times10^{-34}(300/T_g)^{1.25}$ cm^{6}s^{-1}		34
R24	$O+O+O_2\rightarrow O_2+O_2$	$2.56\times10^{-34}(300/T_g)^{0.63}$ cm^{6}s^{-1}		34
R25	$O^-+O_2^*\rightarrow O_2^-+O$	1.0×10^{-10} cm^{3}s^{-1}		31
R26	$O^-+O_2\rightarrow O_3+e$	$5.0\times10^{-12}(300/T_e)^{-0.5}$ cm^{3}s^{-1}		34
R27	$O^-+O_3\rightarrow O_3^-+O$	5.3×10^{-10} cm^{3}s^{-1}		35
R28	$O(^1D)+O_2\rightarrow O+O_2$	$4.8\times10^{-12}\exp(-67/T_g)$ cm^{3}s^{-1}		34
R29	$O(^1D)+O_2\rightarrow O+O_2(^1\Sigma_g^+)$	2.0×10^{-11} cm^{3}s^{-1}		31
R30	$O(^1D)+O\rightarrow 2O$	8.0×10^{-12} cm^{3}s^{-1}		32
R31	$O(^1D)+O_3\rightarrow O_2(^1\Delta g)+O_2$	2.7×10^{-10} cm^{3}s^{-1}		36
R32	$O(^1D)+O_3\rightarrow 2O_2(^1\Delta g)$	2.5×10^{-10} cm^{3}s^{-1}		36
R33	$O(^1D)+O_3\rightarrow 2O+O_2$	1.2×10^{-10} cm^{3}s^{-1}		34
R34	$O(^1D)+O_3\rightarrow 2O_2$	1.2×10^{-10} cm^{3}s^{-1}		34
R35	$O_2^-+O^+\rightarrow O_2+O$	$2.0\times10^{-7}(300/T_g)$ cm^{3}s^{-1}		34
R36	$O_2^-+O_2^+\rightarrow 2O_2$	$2.0\times10^{-7}(300/T_g)$ cm^{3}s^{-1}		34
R37	$O_2(^1\Delta g)+O_3\rightarrow 2O_2+O(^1D)$	1.0×10^{-11} cm^{3}s^{-1}		35
R38	$O_2(^1\Sigma_g^+)+O_3\rightarrow 2O_2+O$	1.5×10^{-11} cm^{3}s^{-1}		35
R39	$O_2^-+O_3\rightarrow O_2+O_3^-$	$6.0\times10^{-10}(300/T_g)^{-0.5}$ cm^{3}s^{-1}		34
R40	$O_2+O^+\rightarrow O_2^++O$	$2.0\times10^{-11}(300/T_g)^{-0.5}$ cm^{3}s^{-1}		32
R41	$O_2(^1\Delta g)+O_2\rightarrow 2O_2$	$2.2\times10^{-18}(T_g/300)^{0.8}$ cm^{3}s^{-1}		32
R42	$O_3+O\rightarrow 2O_2$	$1.5\times10^{-11}\exp(-2250/T_g)$ cm^{3}s^{-1}		28
R43	$O_3^-+O\rightarrow O_2^-+O_2$	3.2×10^{-10} cm^{3}s^{-1}		35
R44	$O_3^-+O_2^+\rightarrow 2O+O_3$	2.0×10^{-7} cm^{3}s^{-1}		34
R45	$He^*+O_2\rightarrow O_2^++He+e$	$2.54\times10^{-10}(300/T_g)^{-0.5}$ cm^{3}s^{-1}		34
R46	$He^++2He\rightarrow He_2^++He$	1.0×10^{-31} cm^{6}s^{-1}		26
R47	$He^*+2He\rightarrow He_2^*+He$	1.6×10^{-32} cm^{6}s^{-1}		37
R48	$He^*+He^*\rightarrow He_2^++e$	1.5×10^{-9} cm^{6}s^{-1}		30
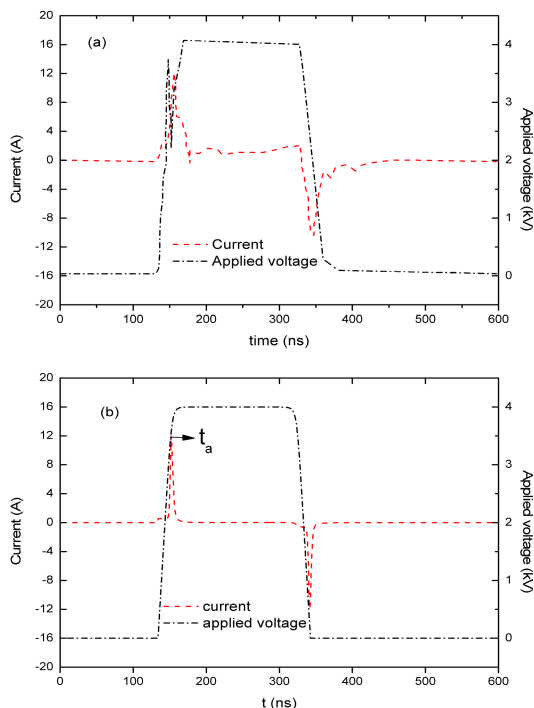
FIGURE 2. Comparison between the (a) experimental discharge current[38] and (b) calculated discharge current in the pulsed DBD in helium oxygen mixture.

the gap width d_g = 0.2 cm. Besides, the pulse width, amplitude and frequency of the applied voltage are fixed at 200 ns, 4 kV, and 5 kHz, respectively, the rising time (= falling time) t_r is less than 20 ns, and oxygen concentration is taken as 0.5%. The discharge current in atmospheric-pressure He/O_2 pulsed DBD has been simulated and prepared with the experiment [38].

Figure 2 displays a comparison between the discharge currents from the experiment and from the present simulation. It can be clearly observed from Fig. 2 that during a single cycle of the applied voltage pulse, there are two discharges, occurring at the rising edge and falling edge of V_a, respectively, and the respective maximum for the two discharge currents from the simulation is approximately equal to that measured in the experiment, which is in reasonable agreement with the experiment of Walsh *et al*. The gap voltage V_g increases with the increase in the voltage amplitude at the rising edge of the voltage pulse. The increasing V_g allows the gas fast breakdown, and thus the rapid increasing discharge current. In the process of the discharge, electrons and ions are accumulated on the dielectric, leading to the increase in the dielectric voltage V_d, and thus the decrease in the V_g (=V_a−V_d). As the V_g decreases, the discharge current decreases rapidly, and then, the first discharge is accomplished. Similarly, the second discharge will occur at the falling edge of the voltage pulse.

Here, it should be pointed out that the discharge current obtained by our model is in smooth behavior and presents short duration, compared to that given by the experiment in Fig. 2(a), which means that the average dissipated power
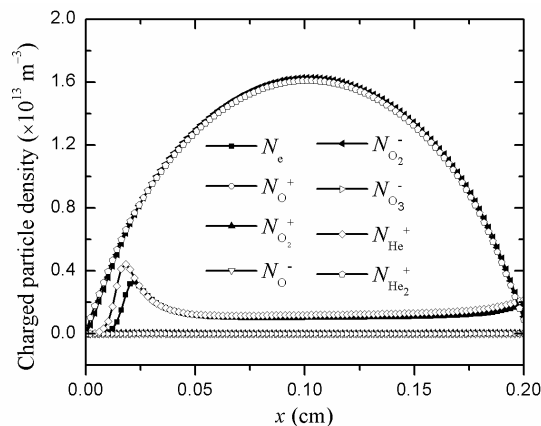

FIGURE 3. Axial distributions of the charged particles at time t_a.

due to our model is slightly low in contrast with that shown by the experiment. In practice, there are many uncontrollable factors impacting the experiment, and also there are stray capacitors between the electrodes and the air. These may induce both large dissipated power in the experiments and the pulse voltage in the jitter, as observed in Fig. 2(a).

Further, Fig. 3 presents the axial distributions of the charged particle densities at the peak of the first discharge t_a shown in Fig. 2 (b). It is clear from Fig. 3 that the dominative positive and negative particles are He_2^+ and O_2^-, and the densities of these two particles are of parabolic axial distribution, presenting the maximum nearly at the central position of the gap, and the densities of He_2^+ and O_2^- are nearly equivalent to each other. This characteristic of distribution of He_2^+ and O_2^- is consistence with the experiment in Lu *et al*. [39].

In this work, the parameters of the discharge structure are set as follows. The thickness and the relative dielectric constant of the dielectric plate is fixed at 0.1 cm and 7.6, respectively. The secondary electron emission coefficient is 0.02. The gap width is set to 0.1 cm. As for the parameters of applied voltage pulse, the V_a is in the range from 3 to 10 kV, the considered t_rs are 50, 100, 300, 500, 700, and 900 ns, and the f varies from 2.5 to 40 kHz.

III. RESULTS AND DISCUSSION
Using the 1-D fluid model and parameters setting mentioned above and with the consideration of the generated particles, the atmospheric-pressure helium/oxygen pulsed DBDs have been calculated, and the effects of oxygen concentrations on the ROS density under different operating conditions are analyzed in detail.

To have a deep understanding of the operating condition dependences of the oxygen concentration effects later on, as an example, Fig. 4 gives the effects of oxygen concentration on the space-averaged densities of the four ROS, i.e., O, O_3, O(^{1}D), and SDO at the time point t_a, as marked in Fig. 2 (b). Based on the setup described in Fig. 1, a positive voltage of 4 kV with the t_r of 100 ns is applied, the pulse width and the frequency f is fixed at 600 ns and 5 kHz, respectively. It is clear from Fig. 4 that for a fixed oxygen
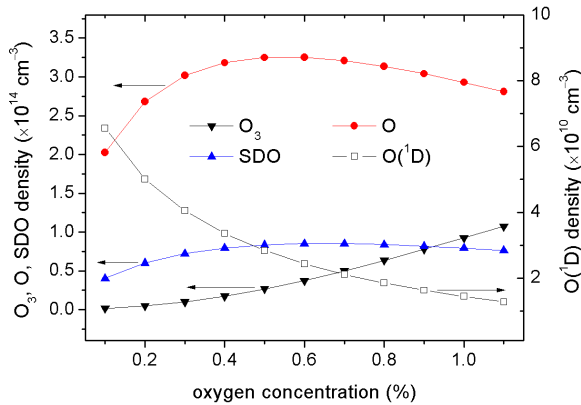
FIGURE 4. Averaged densities of O_3, O, $O(^1D)$, and SDO versus O_2 concentration.

concentration, the averaged O density is evidently large than the three other ROS densities. O density increases with the oxygen concentration at the concentrations below about 0.5%, and then, the O density starts to decrease with increasing oxygen concentration. The oxygen concentration dependence of SDO density is similar to that of O density, and the SDO density reaches its maximum when the concentration is about 0.6%. For the considered oxygen concentrations, the O_3 density increases with the oxygen concentration, and the reverse is true for the $O(^1D)$ density. The reason for this may be shown from the following analysis, namely, the contributions of the reactions to the generation and destruction of the oxygen-related species.

The main reactions generating the O include $e+O_2 \rightarrow O+O(^1D)+e$ (R12), $e+O_2 \rightarrow O+O+e$ (R16), $O(^1D)+O_2 \rightarrow O+O_2$(R28), and $O(^1D)+O_2 \rightarrow O +O_2(^1\Sigma_g^+)$ (R29), and the main reactions inducing the loss of the O include $O+O+He\rightarrow O_2+He$ (R21) and $O+He+O_2 \rightarrow He+O_3$ (R22). To qualitatively explore the contributions of these reactions to the generation and destruction of the O under different oxygen concentrations, Fig. 5 gives the reaction rates of generation and destruction for the O as a function of the oxygen concentration. It can be observed from Fig. 5(a) that the oxygen concentration dependences of the reaction rates present similar characteristics, and for a fixed oxygen concentration, the four reaction sorted in the ascending order of the contributions to generating O are R29, R16, R12, and R28 at the oxygen concentrations above 0.2%. As shown in Fig. 5(b), the contribution of R22 to destructing the O increases basically with the oxygen concentration, while there exists a turning point where the contribution of R21 reaches its maximum. In addition, the dominant reaction for the destruction of the O is R22 at the oxygen concentrations above 0.2%.

It is concluded from Figs. 4 and 5 that on the one hand, the reaction rates for both the generation and the destruction of the O increase with the oxygen concentration at the concentrations below about 0.5%, and the contributions to the O production play the dominant role, leading to the increase in the O density with the oxygen concentration.
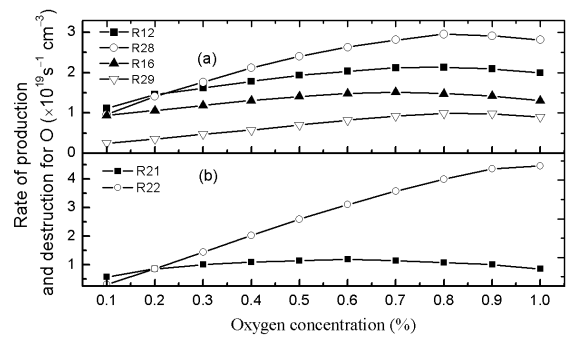

FIGURE 5. Contributions of reactions to the production (a) and destruction (b) of the O as a function of the oxygen concentration.
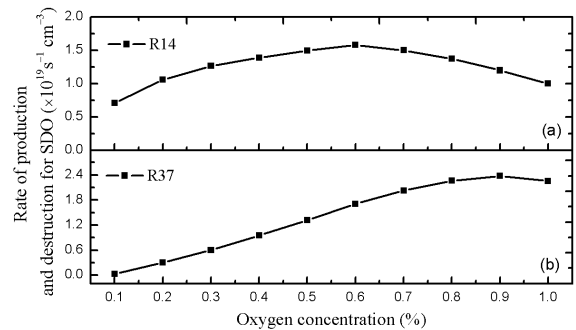

FIGURE 6. Contributions of reactions to the generation (a) and destruction (b) of the SDO as a function of the oxygen concentration.

On the other hand, however, it has been pointed out that the discharge becomes more electronegative and the electron temperature decreases as oxygen concentration is increased from 0.1% to 1% [24], [40], [41]. Consequently, the increase in the oxygen concentration will lead to the existence of more oxygen molecules and more electrons adsorption by oxygen molecules in the discharge gap, which leads to the reduction of the production of electron collision ionization reaction. Therefore, as the oxygen concentration further increases, the reaction rates of the R12 and R16 increase slow and even begin to decrease due to the electronegativity of the oxygen. Besides, as has been shown in Fig. 4, $O(^1d)$ density decreases with the increasing oxygen concentration, resulting in the reaction rates of the R28 and R29 versus the oxygen concentration. Therefore, less contributions of reactions generating the O are obtained with the increase in the oxygen concentration at the concentrations above about 0.5%. On the other hand, the consumption of the O increases due to the increasingly severe R22 for the destruction of the O. Due to the above, the characteristics of the main reactions of generating and destructing the O as a function of the oxygen concentration result in the variation tendency of the O versus oxygen concentration.

As done early, the oxygen concentration dependence of the SDO density will be analyzed qualitatively here. To this end, the reaction rates of production and destruction for SDO as a function of the oxygen concentration have been calculated and presented in Fig. 6. The main reaction generating the
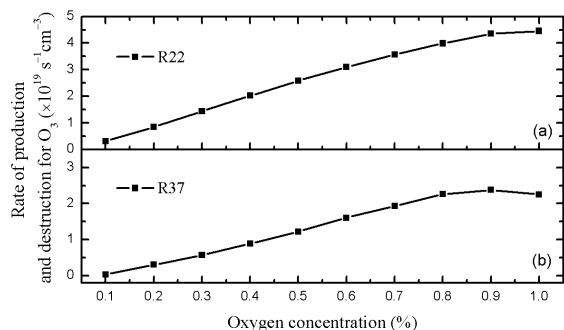
FIGURE 7. Contributions of reactions to the generation (a) and destruction (b) of the O_3 as a function of the oxygen concentration.
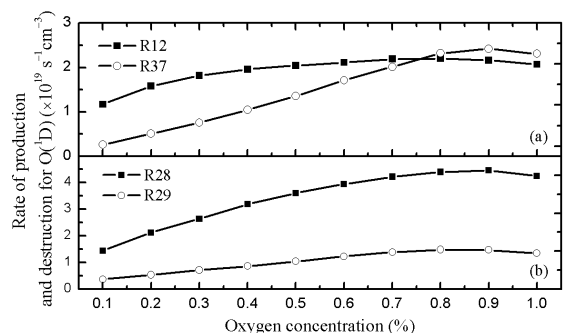

FIGURE 8. Contributions of reactions to the generation (a) and destruction (b) of the $O(^1D)$ as a function of the oxygen concentration.

SDO is $e + O_2 \rightarrow O_2(^1\Delta_g) + e$ (R14), and the main reactions inducing the loss of the SDO is $O_2(^1\Delta_g) + O_3 \rightarrow 2O_2 + O(^1D)$ (R37). It is clear from this figure that the reaction rate of R14 increases with the increase in the oxygen concentration at the concentration below about 0.6%, and then, it decreases as the concentration further increases due to the electronegativity of oxygen. In addition, the reaction rate of R37 basically increases with the increase in the oxygen concentration, mainly because of the increasing O_3 density. Despite that the reaction rate of R37 increases linearly with the increase in the oxygen concentration at the concentrations below about 0.6%, the reaction rate of R14 increases with the oxygen concentration, which induces the increase in the SDO density at the concentrations below about 0.6%. As the oxygen concentration further increases, the decreasing rate of R14 and slow-growing rate of R37 lead to the turning point where the SDO density reaches its maximum.

For the mechanism governing the effect of oxygen concentration on O_3 density, the reaction rates of production and destruction for O_3 as a function of the oxygen concentration have been given in Fig. 7. The main reaction generating the O_3 is $O + He + O_2 \rightarrow He + O_3$ (R22), and the main reactions inducing the loss of the SDO is $O_2(^1\Delta_g) + O_3 \rightarrow 2O_2 + O(^1D)$ (R37). It can be observed from Fig. 7 that the reaction rates of both R22 and R37 nearly increases with the oxygen concentration. In addition, for a fixed oxygen concentration, the rate of R22 is larger than that of R37. These lead to the increase in the O_3 density with the oxygen concentration.

Similarly, Fig. 8 illustrates the reaction rates of production and destruction for $O(^1D)$ as a function of the oxygen concentration. The main reaction generating the $O(^1D)$ include $e + O_2 \rightarrow O + O(^1D) + e$ (R12) and $O_2(^1\Delta_g) + O_3 \rightarrow 2O_2 + O(^1D)$ (R37), and the main reactions inducing the loss of the $O(^1D)$ include $O(^1D) + O_2 \rightarrow O + O_2$ (R28) and $O(^1D) + O_2 \rightarrow O + O_2(^1\Sigma_g^+)$ (R29). It is clearly seen that from Fig. 8(a) that the R12 plays a dominant role in generating the $O(^1D)$ when increasing the oxygen concentration at the concentrations below about 0.7%, while the larger contribution to generating $O(^1D)$ is R28 the when further increasing the oxygen concentration. In addition, both the reaction rates of R12 and R37 increase with the increasing oxygen concentration, and then, they decrease as the concentration further increases. This implies that the rates of the R12 and R37 will be strengthened within a certain range of the oxygen concentration because of the electronegativity of the oxygen. In Fig. 8(b), it is clear that for a fixed oxygen concentration, the rate of R28 is evidently large that that of R29, indicating that the R28 is the major contribution to destructing the $O(^1D)$. Besides, both the rates of R28 and R29 increase with the increase in the oxygen concentration at the concentrations below about 0.9% and 0.8%, respectively. Combining Fig. 8(a) and (b), the increasing oxygen concentration has an inhibitory effect on the R12 at the concentration above about 0.7%. On the other hand, the contribution of R28 to destructing the $O(^1D)$ increases as the oxygen concentration increases, despite of the increasing contribution of R37 to generating the $O(^1D)$. The increasingly destruction for $O(^1D)$ due to the more and more severe R28 results in the decrease in the $O(^1D)$ density with the increase in the oxygen concentration.

In fact, the addition of oxygen will result in the generation and loss of the ROS, and the increasingly oxygen concentration added to the working gas will weaken the plasmas, leading to the saturation and decrease in ROS production. It is, therefore, indicated that the oxygen concentration dependences of different ROS densities are different from each other due to the different reaction mechanisms of generation and loss of the ROS.

After knowing about the oxygen concentration dependences of the four ROS densities, the operating conditions dependences of the oxygen concentration effects of the ROS density will then be investigated in detail.

The applied voltage amplitude V_a is one of the important parameters to characterize the pulse power supply, and the characteristics and ROS density of the pulsed DBD in He/O_2 mixture will be significantly affected by changing the V_a. Here, the pulse width and t_r are fixed at 600 and 100 ns, respectively, the frequency f is set to 5 kHz, The effect of V_a on optimal O_2 concentration has been investigated, and the considered V_a varies from 3 to 10 kV.

Figure 9 gives the averaged densities of O, SDO, O_3, and $O(^1D)$ as a function of oxygen concentration under the applied voltage amplitude V_a in the range from 3 to 10 kV. It can be clearly seen that for a fixed oxygen concentration,
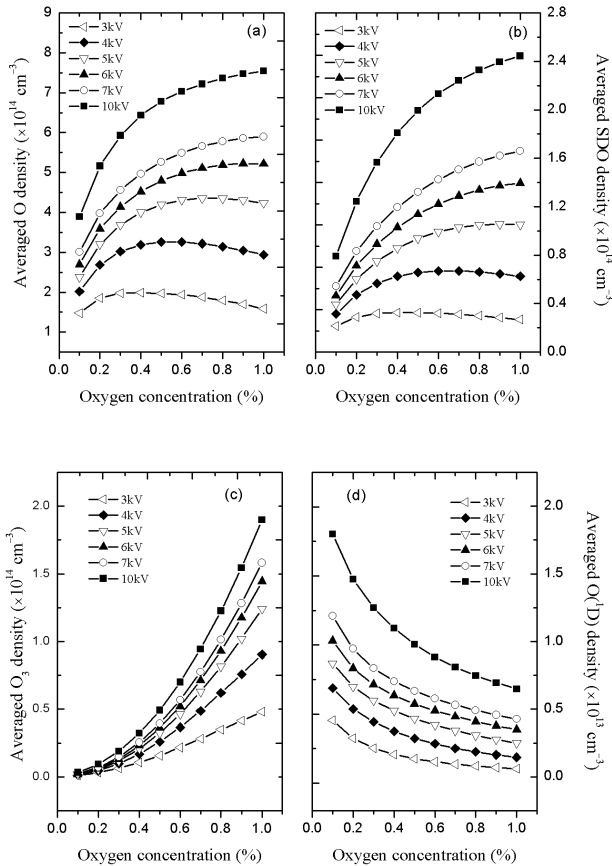
FIGURE 9. Averaged densities of O (a), SDO (b), O$_3$ (c), and O(^{1}D) (d) as a function of oxygen concentration under different V_a.
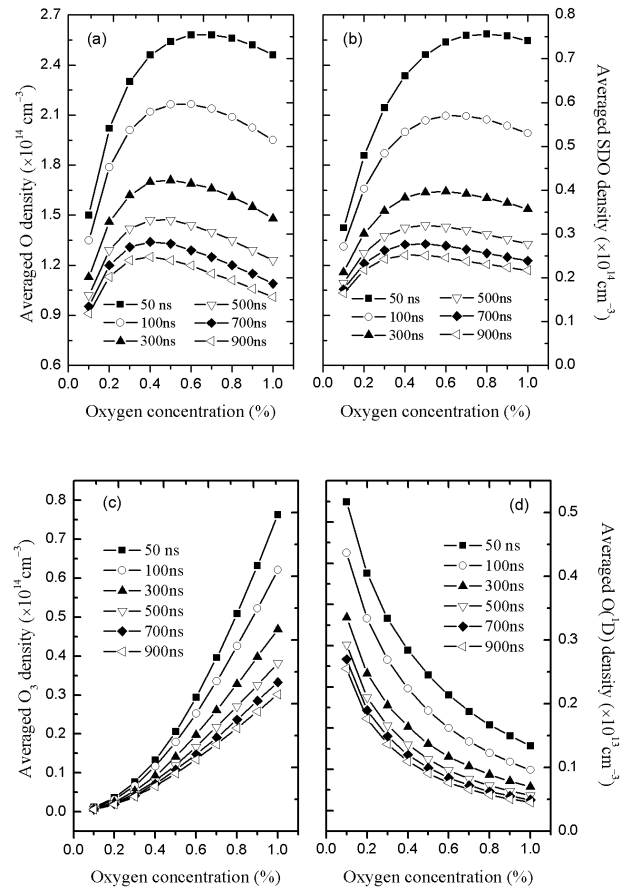

FIGURE 10. Averaged densities of O (a), SDO (b), O$_3$ (c), and O(^{1}D) (d) as a function of oxygen concentration under different t_r.

the averaged densities of the four ROS increase with the applied voltage amplitude V_a. In Fig. 9(a), it is clear that the averaged O density reaches its maximum at the oxygen concentration is about 0.3% when the applied voltage amplitude V_a of 3 kV is applied, and the maximum moves towards high oxygen concentration when keeping increasing the V_a, namely, the averaged O density reaches its maximum at the oxygen concentration is about 0.5% and 1% when applying the voltage amplitude V_a of 4 kV and 6 kV, respectively. For the averaged SDO density shown in Fig. 9(b), the oxygen concentration dependences of the SDO density are the same as those presented in Fig. 9(a). It is observed from Fig. 9(c) that the averaged O$_3$ density increases monotonically with the oxygen concentration. Besides, the effect of the applied voltage amplitude on the O$_3$ density becomes much more evident at higher oxygen concentrations. Regarding the O(^{1}D) density versus oxygen concentration shown in Fig. 9(d), the averaged O(^{1}D) density decreases with the oxygen concentration. The reason for this may be shown by the following analyses.

The increase in the applied voltage amplitude the will increase the power coupled to the plasma and thus the density of reactive oxygen particles. On the other hand, despite that e+O$_2$ →O+O(^{1}D)+e (R12) and e+O$_2$ →O+O+e (R16) for the generation of O and e+O$_2$ →O$_2$($^1\Delta_g$)+e (R14) for

the generation of SDO will be weakened due to the electronegativity of the oxygen with the increase in the oxygen concentration, the increasing V_a will bring more high-energy electrons, thus leading to more severe R12, R16, and R14. Consequently, the turning point where the averaged densities of the O and SDO reaches their maximum moves towards high oxygen concentration when keeping increasing the V_a, respectively. In the meanwhile, the increasing O density will make the O + He + O$_2$ → He + O$_3$ (R22) severe, thus more O$_3$ is generated at higher voltage amplitudes and higher oxygen concentrations, making the effect of the V_a on the O$_3$ density much more evident at higher oxygen concentrations. As for the O(^{1}D), O(^{1}D) + O$_2$ → O + O$_2$ (R28) causes the O(^{1}D) density decreasing with the oxygen concentration, but the severity of R28 depends on the reactant density and reaction rate coefficient, these two factors have nothing to do with electron energy. Therefore, the variation trend of the averaged O(^{1}D) density with oxygen concentration is nearly not affected by the voltage amplitude, namely, the effects of the oxygen concentration on the O(^{1}D) density are similar to each other under different voltage amplitudes.

The rising time of the applied voltage pulse t_r is another crucial parameter affecting the plasma characteristics and ROS density. Here, the amplitude, pulse width and the
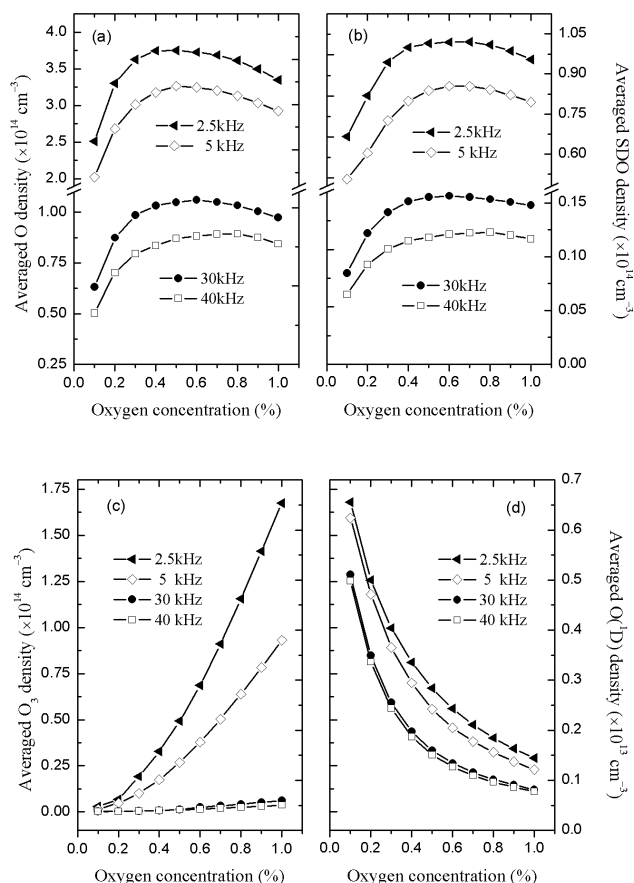
FIGURE 11. Averaged densities of O (a), SDO (b), O_3 (c), and $O(^1D)$ (d) as a function of oxygen concentration under different f.

frequency of the applied voltage is fixed at 4 kV, 2 μs and 5 kHz, respectively. The considered t_r varies from 50 to 900 ns.

Figure 10 presents the averaged densities of O, SDO, O_3, and $O(^1D)$ as a function of oxygen concentration under the rising time of the applied voltage t_r in the range from 50 to 900 ns.

It can be clearly seen that for a fixed oxygen concentration, the averaged densities of the four ROS decreases with the increase in the rising time t_r. In addition, As can be seen from Fig. 10(a) and (b), the averaged density of O and SDO reaches their maximum at the oxygen concentration is about 0.7% when the t_r is set to 50 ns. When keeping increasing the t_r to 100 ns, the optimal oxygen concentration where the averaged density of O and SDO reaches their maximum is about 0.5%. The averaged density of O and SDO reaches their maximum at the oxygen concentration is about 0.4% when the t_r is further increased to 900 ns. A clear indication is that the optimal oxygen concentration moves towards the lower concentration with the increasing rising time of the applied voltage pulse t_r. It is observed from Fig. 10(c) and (d) that the averaged O_3 density increases monotonically with the oxygen concentration, while the averaged $O(^1D)$ density decreases with the oxygen concentration. In addition, the effect of t_r on the averaged O_3 density under the lower

oxygen concentration is unobvious, and the effect becomes profound with the increase in oxygen concentration. As for $O(^1D)$ density, the variation trend of the averaged $O(^1D)$ density versus oxygen concentration is hardly affected by the t_r. The reason for this can be ascribed to the reason similar to that due to the V_a. Combing Figs. 9 and 10, it is concluded that whether increasing V_a or decreasing t_r will increase the density of the electrons with high energy and thus improve the efficiency of the discharge, leading to the increase in the ROS density.

As regards the frequency f of applied voltage pulse, the considered f is in the range from 2.5 to 10 kHz. In addition, the amplitude of the applied voltage is fixed at 4 kV, and the rising time t_r and pulse width of the applied voltage is set to 100 and 600 ns, respectively. Figure 11 displays the averaged densities of O, SDO, O_3, and $O(^1D)$ as a function of oxygen concentration under the various frequency f. As shown in Fig. 11, for a fixed oxygen concentration, the averaged densities of the four ROS decreases with the increase in the frequency f. In the context of the fixed pulse width, as the frequency f increases, the pulse-off time becomes shorter. This leads to less recombination between the electrons and other species and in turn more seed electrons remaining in the gap. The electrons accumulated on the dielectric become more, which gives rise to the decrease in the breakdown voltage of the gap. Therefore, the discharge becomes increasingly weak and the resultant averaged densities of the four ROS decreases with the increase in the frequency f. Here, it should be pointed out that the behaviors of the four ROS densities versus the f presented in Fig. 11 only occurs within the frequency range considered in this work. In fact, as the frequency f further increases and becomes higher than the considered f, more and more seed electrons and other species will still remain in the gap in spite of more electrons accumulated on the dielectric as well as its effect of decreasing the breakdown voltage of the gap. The abundant collisions of these remaining electrons with other particles cause the strong discharge. Consequently, the discharge becomes increasingly strong as the frequency further increases.

It can also be seen from Fig. 11(a) and (b) that the optimal oxygen concentration where the averaged density of O and SDO reaches their maximum is about 0.4% when the frequency f of 2.5 kHz is applied, and the optimal oxygen concentration moves towards the higher concentration with the increase in the f. The averaged density of O and SDO reaches their maximum at the oxygen concentration is about 0.8% when applying the frequency f to 40 kHz. The increasing f causes less recombination between the electrons and other species, a clear indication is that the proportion of electrons participating in R12, R16, and R14 increases with the increase in the f. Therefore, this leads that the turning point where the averaged densities of the O and SDO reaches their maximum moves towards high oxygen concentration. Combining Fig. 11(c) and (d), it is clear that the averaged O_3 density increases monotonically with the oxygen concentration, but the reverse is true for the averaged $O(^1D)$ density.

Besides, the effect of the frequency on the averaged O_3 density under the lower oxygen concentration is inconspicuous, and the effect becomes profound with the increase in oxygen concentration. As for $O(^1D)$ density, the variation trend of the averaged $O(^1D)$ density versus oxygen concentration is almost the same under different frequencies. In addition, at the higher frequencies of 30 kHz and 40 kHz, the effect of oxygen concentration on the averaged densities of O_3 and $O(^1D)$ is hardly affected by frequency.

IV. CONCLUSION

In this work, the effects of oxygen concentration on ROS density under different operating conditions in the atmospheric-pressure helium/oxygen pulsed DBDs have been numerically investigated based on a 1-D fluid model. Here, the operating conditions is the amplitude, rising time, and frequency of the applied voltage pulse, and the considered oxygen concentration is in the range from 0.1% to 1%. The present work presents the following significant results.

For a given operating condition, the averaged O density is evidently large than the three other ROS densities. There exists a turning point where the averaged densities of O and SDO reach their maximum with the increase in the oxygen concentration. As regards the averaged densities of O_3 and $O(^1D)$, the O_3 density increases with the oxygen concentration, but the reverse is true for the $O(^1D)$ density.

The averaged densities of the four ROS are increased by means of increasing the voltage amplitude, decreasing the rising time of the voltage pulse, or reducing the frequency. In addition, for the considered oxygen concentration in the range from 0.1% to 1%, the turning point for the averaged densities of O and SDO moves towards the higher oxygen concentration with the increase in the voltage amplitude, decrease in the rising time of the pulse, or increase in the frequency. Regarding the O_3 density, the effect of the operating conditions on the averaged O_3 density is unobvious under lower oxygen concentrations, and it is increasingly affected by the operating conditions with the oxygen concentration increased. As for the $O(^1D)$ density, the variation trend of the averaged $O(^1D)$ density as a function of oxygen concentration is hardly affected by the operating conditions.

The generation of the ROS will be weakened due to the electronegativity of oxygen with the increase in the oxygen concentration, and thus, a proper high oxygen concentration needs to be considered, leading to enhance the plasma chemistry. In addition, the effects of oxygen concentrations are different for different operating conditions. Thus, it is essential to select the appropriate oxygen concentration according to the actual operating conditions, so as to obtain the abundant reactive oxygen species.

REFERENCES

[1] J. Kim, M. Katsurai, D. Kim, and H. Ohsaki, "Microwave-excited atmospheric-pressure plasma jets using a microstrip line," *Appl. Phys. Lett.*, vol. 93, no. 19, Nov. 2008, Art. no. 191505. doi: 10.1063/1.3025841.

[2] Z. Fang, X. Xie, J. Li, H. Yang, Y. Qiu, and E. Kuffel, "Comparison of surface modification of polypropylene film by filamentary DBD at atmospheric pressure and homogeneous DBD at medium pressure in air," *J. Phys. D, Appl. Phys.*, vol. 42, no. 8, Mar. 2009, Art. no. 085204. doi: 10.1088/0022-3727/42/8/085204.

[3] T. Shao, C. Zhang, K. Long, D. Zhang, J. Wang, P. Yan, and Y. Zhou, "Surface modification of polyimide films using unipolar nanosecond-pulse DBD in atmospheric air," *Appl. Surf. Sci.*, vol. 256, no. 12, pp. 3888–3894, Apr. 2010. doi: 10.1016/j.apsusc.2010.01.045.

[4] D. Shaw, A. West, J. Bredin, and E. Wagenaars, "Mechanisms behind surface modification of polypropylene film using an atmospheric-pressure plasma jet," *Plasma Sour. Sci. Technol.*, vol. 25, no. 6, Oct. 2016, Art. no. 065018. doi: 10.1088/0963-0252/25/6/065018.

[5] J. Foster, B. S. Sommers, S. N. Gucker, I. M. Blankson, and G. Adamovsky, "Perspectives on the interaction of plasmas with liquid water for water purification," *IEEE Trans. Plasma Sci.*, vol. 40, no. 5, pp. 1311–1323, May 2012. doi: 10.1109/TPS.2011.2180028.

[6] D. Mei, X. Zhu, Y.-L. He, J. D. Yan, and X. Tu, "Plasma-assisted conversion of CO_2 in a dielectric barrier discharge reactor: Understanding the effect of packing materials," *Plasma Sour. Sci. Technol.*, vol. 24, no. 1, Dec. 2015. doi: Art. no. 015011. doi: 10.1088/0963-0252/24/1/015011.

[7] A. A. H. Mohamed, S. M. A. Shariff, S. A. Ouf, and M. Benghanem, "Atmospheric pressure plasma jet for bacterial decontamination and property improvement of fruit and vegetable processing wastewater," *J. Phys. D, Appl. Phys.*, vol. 49, no. 19, Apr. 2016, Art. no. 195401. doi: 10.1088/0022-3727/49/19/195401.

[8] D. Mei and X. Tu, "Atmospheric pressure non-thermal plasma activation of CO_2 in a packed-bed dielectric barrier discharge reactor," *ChemPhysChem*, vol. 18, no. 22, pp. 3253–3259, Nov. 2017. doi: 10.1002/cphc.201700752.

[9] A. Vincent-Randonnier, S. Larigaldie, P. Magre, and V. Sabel'nikov, "Plasma assisted combustion: Effect of a coaxial DBD on a methane diffusion flame," *Plasma Sour. Sci. Technol.*, vol. 16, no. 1, pp. 149–160, Dec. 2007. doi: 10.1088/0963-0252/16/1/020.

[10] Y. Ju and W. Sun, "Plasma assisted combustion: Dynamics and chemistry," *Process Energy Combustion Sci.*, vol. 48, pp. 21–83, Jun. 2015. doi: 10.1016/j.pecs.2014.12.002.

[11] M. Laroussi, "Low-temperature plasmas for medicine?" *IEEE Trans. Plasma Sci.*, vol. 37, no. 6, pp. 714–725, Jun. 2009. doi: 10.1109/TPS.2009.break2017267.

[12] A. V. Nastuta, V. Pohoata, and I. Topala, "Atmospheric pressure plasma jet—Living tissue interface: Electrical, optical, and spectral characterization," *J. Appl. Phys.*, vol. 113, no. 18, May 2013, Art. no. 183302. doi: 10.1063/1.4804319.

[13] M. Keidar and E. Robert, "Preface to special topic: Plasmas for medical applications," *Phys. Plasmas*, vol. 22, no. 12, Oct. 2015, Art. no. 121901. doi: 10.1063/1.4933406.

[14] X. Lu and M. Laroussi, "Dynamics of an atmospheric pressure plasma plume generated by submicrosecond voltage pulses," *J. Appl. Phys.*, vol. 100, no. 6, Sep. 2006, Art. no. 063302. doi: 10.1063/1.2349475.

[15] X. Lu and M. Laroussi, "Electron density and temperature measurement of an atmospheric pressure plasma by millimeter wave interferometer," *Appl. Phys. Lett.*, vol. 92, no. 5, Feb. 2008, Art. no. 051501. doi: 10.1063/1.2840194.

[16] S. Zhang, W.-C. Wang, P.-C. Jiang, D.-Z. Yang, L. Jia, and S. Wang, "Comparison of atmospheric air plasmas excited by high-voltage nanosecond pulsed discharge and sinusoidal alternating current discharge," *J. Appl. Phys.*, vol. 114, no. 16, Oct. 2013, Art. no. 163301. doi: 10.1063/1.4825053.

[17] X. Lu, G. V. Naidis, M. Laroussi, S. Reuter, D. B. Graves, and K. Ostrikov, "Reactive species in non-equilibrium atmospheric-pressure plasmas: Generation, transport, and biological effects," *Phys. Rep.*, vol. 630, no. 4, pp. 1–84, May 2016. doi: 10.1016/j.physrep.2016.03.003.

[18] G. Lloyd, G. Friedman, S. Jafri, G. Schultz, A. Fridman, and K. Harding, "Gas plasma: Medical uses and developments in wound care," *Plasma Processes Polymers*, vol. 7, nos. 3–4, pp. 194–211, Mar. 2010. doi: 10.1002/ppap.200900097.

[19] D. Lee, J. M. Park, S. H. Hong, and Y. Kim, "Numerical simulation on mode transition of atmospheric dielectric barrier discharge in helium-oxygen mixture," *IEEE Trans. Plasma Sci.*, vol. 33, no. 2, pp. 949–957, Apr. 2005. doi: 10.1109/tps.2005.844493.

[20] N. H. Alshraiedeh, M. Y. Alkawareek, S. P. Gorman, W. G. Graham, and B. F. Gilmore, "Atmospheric pressure, nonthermal plasma inactivation of MS2 bacteriophage: Effect of oxygen concentration on virucidal activity," *J. Appl. Microbiology*, vol. 115, no. 6, pp. 1420–1426, Dec. 2013. doi: 10.1111/jam.12331..

[21] Y. Song, D. Liu, L. Ji, W. Wang, P. Zhao, C. Quan, J. Niu, and X. Zhang, "The inactivation of resistant Candida albicans in a sealed package by cold atmospheric pressure plasmas," *Plasma Processes Polymers*, vol. 9, no. 1, pp. 17–21, Jan. 2011. doi: 10.1002/ppap.201100075.

[22] W. Xiaolong, T. Zhenyu, P. Jie, and C. Xinxian, "Effects of oxygen concentration on pulsed dielectric barrier discharge in helium-oxygen mixture at atmospheric pressure," *Plasma Sci. Technol.*, vol. 18, no. 8, pp. 837–843, 2016. doi: 10.1088/1009-0630/18/8/08.

[23] J. Pan, Z. Tan, Y. Liu, G. Pan, and X. Wang, "Effects of oxygen concentration on atmospheric-pressure pulsed dielectric barrier discharges in argon/oxygen mixture," *Phys. Plasmas*, vol. 22, no. 9, Sep. 2015, Art. no. 093515. doi: 10.1063/1.4931740.

[24] G. Pan, Z. Tan, J. Pan, X. Wang, and C. Shan, "A comparative study on the frequency effects of the electrical characteristics of the pulsed dielectric barrier discharge in He/O_2 and in Ar/O_2 at atmospheric pressure," *Phys. Plasmas*, vol. 23, no. 4, Apr. 2016, Art. no. 043508. doi: 10.1063/1.4946777.

[25] J. He and Y. Zhang, "Modeling study on the generation of reactive oxygen species in atmospheric radio-frequency helium–oxygen discharges," *Plasma Processes Polymers*, vol. 9, no. 9, pp. 919–928, Sep. 2012. doi: 10.1002/ppap.201200067.

[26] S. Rauf and M. J. Kushner, "Dynamics of a coplanar-electrode plasma display panel cell. I. Basic operation," *J. Appl. Phys.*, vol. 85, no. 7, pp. 3460–3469, Mar. 1999. doi: 10.1063/1.369703.

[27] Q. Wang, D. J. Economou, and V. M. Donnelly, "Simulation of a direct current microplasma discharge in helium at atmospheric pressure," *J. Appl. Phys.*, vol. 100, no. 2, Jul. 2006, Art. no. 023301. doi: 10.1063/1.2214591.

[28] R. Deloche, P. Monchicourt, M. Cheret, and F. Lambert, "High-pressure helium afterglow at room temperature," *Phys. Rev. A, Gen. Phys.*, vol. 13, no. 3, pp. 1140–1176, Mar. 1976. doi: 0.1103/PhysRevA.13.1140.

[29] Y. B. Golubovskii, V. A. Maiorov, J. Behnke, and J. F. Behnke, "Modelling of the homogeneous barrier discharge in helium at atmospheric pressure," *J. Phys. D, Appl. Phys.*, vol. 36, no. 1, pp. 39–49, Dec. 2003. doi: 10.1088/0022-3727/36/1/306.

[30] S. Kim, M. A. Lieberman, A. J. Lichtenberg, and J. T. Gudmundsson, "Improved volume-averaged model for steady and pulsed-power electronegative discharges," *J. Vac. Sci. Technol. A*, vol. 24, no. 6, pp. 2025–2040, Oct. 2006. doi: 10.1116/1.2345645.

[31] V. Léveillé and S. Coulombe, "Design and preliminary characterization of a miniature pulsed RF APGD torch with downstream injection of the source of reactive species," *Plasma Sour. Sci. Technol.*, vol. 14, no. 3, pp. 467–476, May 2005. doi: 10.1088/0963-0252/14/3/008.

[32] J. T. Gudmundsson, I. G. Kouznetsov, K. K. Patel, and M. A. Lieberman, "Electronegativity of low-pressure high-density oxygen discharges," *J. Phys. D, Appl. Phys.*, vol. 34, no. 7, pp. 1100–1109, 2001. doi: 10.1088/0022-3727/34/7/312.

[33] D. S. Stafford and M. J. Kushner, "$O_2(^1\triangle)$ production in He/O_2 mixtures in flowing low pressure plasmas," *J. Appl. Phys.*, vol. 96, no. 5, pp. 2451–2465, 2004. doi: 10.1063/1.1768615.

[34] F. J. Gordillo-Vázquez, "Air plasma kinetics under the influence of sprites," *J. Phys. D, Appl. Phys.*, vol. 41, no. 23, Nov. 2008, Art. no. 234016. doi: 10.1088/0022-3727/41/23/234016.

[35] S. Hadi-Ziane, B. Held, P. Pignolet, R. Peyrous, and C. Coste, "Ozone generation in an oxygen-fed wire-to-cylinder ozonizer at atmospheric pressure," *J. Phys. D, Appl. Phys.*, vol. 25, no. 4, pp. 677–685, 1992. doi: 10.1088/0022-3727/25/4/014.

[36] D. L. Baulch, R. A. Cox, P. J. Crutzen, R. F. Hampson, J. A. Kerr, J. Troe, and R. T. Watson, "Evaluated kinetic and photochemical data for atmospheric chemistry: Supplement I CODATA task group on chemical kinetics," *J. Phys. Chem. Reference Data*, vol. 11, no. 2, pp. 327–496, Oct. 1982. doi: 10.1063/1.555664.

[37] C. Soria, F. Pontiga, and A. Castellanos, "Plasma chemical and electrical modelling of a negative DC corona in pure oxygen," *Plasma Sour. Sci. Technol.*, vol. 13, no. 1, pp. 95–107, Nov. 2004. doi: 10.1088/0963-0252/13/1/012.

[38] J. L. Walsh, D. X. Liu, F. Iza, M. Z. Rong, and M. G. Kong, "Contrasting characteristics of sub-microsecond pulsed atmospheric air and atmospheric pressure helium–oxygen glow discharges," *J. Phys. D, Appl. Phys.*, vol. 43, no. 3, Jan. 2010, Art. no. 032001. doi: 10.1088/0022-3727/43/3/032001.

[39] X. Lu, T. Ye, Y. Cao, Z. Sun, Q. Xiong, Z. Tang, Z. Xiong, J. Hu, Z. Jiang, and Y. Pan, "The roles of the various plasma agents in the inactivation of bacteria," *J. Appl. Phys.*, vol. 104, Sep. 2008, Art. no. 053309.

[40] S.-Z. Li, Q. Wu, J. Zhang, D. Wang, and H. S. Uhm, "Development of an atmospheric-pressure homogeneous and cold Ar/O_2 plasma source operating in glow discharge," *Phys. Plasmas*, vol. 17, no. 6, Jun. 2010, Art. no. 063506. doi: 10.1063/1.3447877.

[41] S.-Z. Li, Q. Wu, W. Yan, D. Wang, and H. S. Uhm, "Influence of oxygen traces on an atmospheric-pressure radio-frequency capacitive argon plasma discharge," *Phys. Plasmas*, vol. 18, no. 10, Oct. 2011, Art. no. 103502. doi: 10.1063/1.3643224.

XIAOLONG WANG received the M.S. and Ph.D. degrees in electrical engineering from Shandong University, in 2009 and 2015, respectively, where he is currently an Instructor.

His current research interest include atmospheric-pressure pulsed discharges and low-temperature plasmas.

YADI LIU received the B.E. degree in electrical engineering from the China University of Mining and Technology, Xuzhou, China, in 2013. He is currently pursuing the Ph.D. degree with Shandong University, Jinan, China.

His current research interest includes cold atmospheric pressure plasma jets and their biomedical applications.

ZHENYU TAN received the B.S. degree in industrial automation from the Guizhou Institute of Technology, Guiyang, China, in 1982, the M.S. degree in industrial automation from the Shandong University of Technology, Jinan, China, in 1990, and the Ph.D. degree in optical engineering from Shandong University, Jinan, China, in 2004.

His research interests include radiation effects in organic materials and insulators, the theory and modeling of gas discharge physics, and electromagnetic compatibility.

LILI CHANG received the B.S. and M.S. degrees from Northeastern University and the Ph.D. degree from the Dalian University of Technology. She held a postdoctoral position at the Korea Institute of Materials Science and the Beijing University of Technology.

Since 2012, she joined the School of Materials Science and Engineering, Shandong University. Her research interest includes microstructures and mechanical properties of nonferrous metals.

• • •